

# RF-3DGS: Wireless Channel Modeling with Radio Radiance Field and 3D Gaussian Splatting

Lihao Zhang, *Student Member, IEEE*, Haijian Sun, *Senior Member, IEEE*, Samuel Berweger, Camillo Gentile, *Member, IEEE*, and Rose Qingyang Hu, *Fellow, IEEE*

**Abstract**—Precisely modeling radio propagation in complex environments has been a significant challenge, especially with the advent of 5G and beyond networks, where managing massive antenna arrays demands more detailed information. Traditional methods, such as empirical models and ray tracing, often fall short, either due to insufficient details or because of challenges for real-time applications. Inspired by the newly proposed 3D Gaussian Splatting method in the computer vision domain, which outperforms other methods in reconstructing optical radiance fields, we propose RF-3DGS, a novel approach that enables precise site-specific reconstruction of radio radiance fields from sparse samples. RF-3DGS can render radio spatial spectra at arbitrary positions within 2 ms following a brief 3-minute training period, effectively identifying dominant propagation paths. Furthermore, RF-3DGS can provide fine-grained Spatial Channel State Information (Spatial-CSI) of these paths, including the channel gain, the delay, the angle of arrival (AoA), and the angle of departure (AoD). Our experiments, calibrated through real-world measurements, demonstrate that RF-3DGS not only significantly improves reconstruction quality, training efficiency, and rendering speed compared to state-of-the-art methods, but also holds great potential for supporting wireless communication and advanced applications such as Integrated Sensing and Communication (ISAC). Code and dataset will be available at <https://github.com/SunLab-UGA/RF-3DGS>.

**Index Terms**—Wireless Channel Modeling, 3D Gaussian Splatting, Radio Radiance Field, Digital Twin

## I. INTRODUCTION

### A. Wireless Channel Modeling

Wireless communication systems facilitate the exchange of information carried by Electromagnetic (EM) waves between a physically separated Transmitter (Tx) and Receiver (Rx). As EM waves propagate from the Tx to the Rx, they undergo various effects, including reflection, diffraction, refraction, and scattering. Consequently, these waves may reach the Rx via

multiple paths, and each path is characterized by its own set of channel properties, known as a multipath component (MPC). In the context of 5G and the upcoming 6G Multiple-Input and Multiple-Output (MIMO) networks, the antenna array size is expected to grow to thousands of elements. This expansion requires the efficient spatial management of such large arrays, thereby mitigating the increasing computational complexity associated with pilot-based estimation as the array size increases [1], [2]. This management, in turn, requires the Spatial Channel State Information (Spatial-CSI) [3], which include not only the traditional channel gain and delay of each MPC, but also the angle of departure (AoD), angle of arrival (AoA), and polarization. Meeting this requirement poses a significant challenge for wireless channel modeling.

Over the years, various methods for wireless channel modeling have been developed. The empirical models [4], [5], although effective for providing coarse-grained path loss information over large distances (from hundreds of meters to tens of kilometers), fail to capture the finer details such as the spatial information of the MPCs. Computational Electromagnetics (CEM) methods [6], [7], while being powerful for small-scale modeling, such as antenna design and near-field communication [8], [9], are computationally impractical for a wider range of applications. Ray tracing, positioned between these two approaches, offers a potential solution by approximating radio waves using ray concepts [10], [11], [12]. However, ray tracing is still limited by its high computational complexity and stringent environmental data requirements (e.g., 3D modeling and surface properties), making it unsuitable for more general and real-time applications.

For modeling wireless channel using ray tracing methods, a similar trend has emerged in the Computer Vision (CV) domain for 3D scene reconstruction, where volume rendering techniques [13] are employed based on photographs to optimize scene representations [14], [15], [16]. These representations typically capture the optical radiance emitted from object surfaces towards the camera, thereby enabling novel view synthesis and environment reconstruction. In this process, the optical radiance is modeled as a group of rays passing through each pixel to the camera, similar to how wireless channels are modeled by a group of MPCs arriving at the Rx from different AoAs. This similarity suggests that CV techniques could offer valuable insights for enhancing radio wave propagation modeling.

A recent pioneering work on CV reconstruction is Neural Radiance Field (NeRF) [14], which achieves exceptional synthesis quality with sparse input. Despite its groundbreaking

L. Zhang and H. Sun (lihao.zhang@uga.edu, hsun@uga.edu) are with the School of Electrical and Computer Engineering, University of Georgia, Athens, GA, 30602 USA.

S. Berweger (samuel.berweger@nist.gov) is with the RF Technology Division, National Institute of Standards and Technology, Boulder, CO, 80305 USA.

C. Gentile (camillo.gentile@nist.gov) is with the Wireless Networks Division, National Institute of Standards and Technology, Gaithersburg, MD, 20899 USA.

R. Q. Hu (rosehu@vt.edu) is with Department of Electrical and Computer Engineering, Utah State University, Logan, UT, 84341 USA.

Certain commercial equipment, instruments, or materials are identified in this paper in order to specify the experimental procedure adequately. Such identification is not intended to imply recommendation or endorsement by NIST, nor is it intended to imply that the materials or equipment identified are necessarily the best available for the purpose.

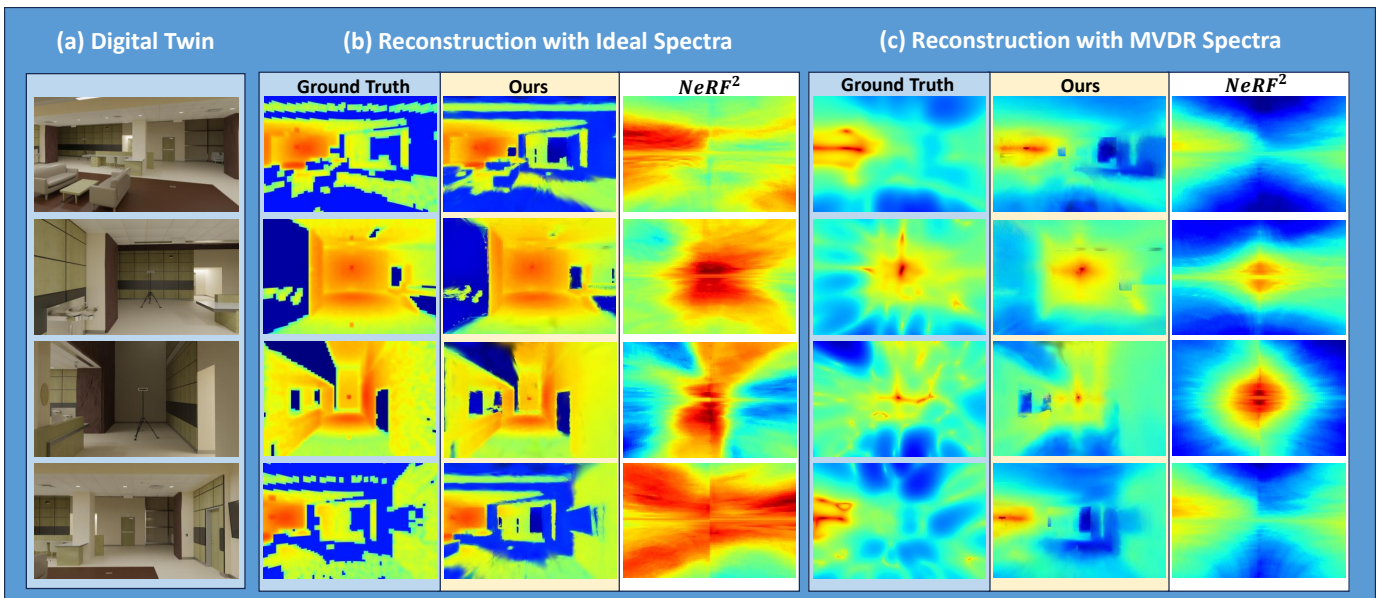


Fig. 1. Reconstructed radio spatial spectra. This figure compares the digital twin, the training ground truth, and the spectra reconstructed by our method and  $NeRF^2$ . (a) shows the digital twin’s visual photograph. (b) illustrates the group with ideal spectra generated by an ideal array pattern (see Fig 8). (c) presents the group with more practical MVDR spectra generated by an  $8 \times 8$  patch antenna array.

results, NeRF has notable limitations, including long training times (up to tens of hours), slow inference times (several seconds). More importantly, its implicit neural network representation requires exhaustive querying of the scene to obtain geometric information. Recently, 3D Gaussian Splatting (3DGS) [17] has emerged as an alternative, achieving higher reconstruction quality with significantly reduced training times (tens of minutes) and much higher inference speeds (less than 10 ms). Over the past year, substantial research has built upon 3DGS, exploring applications such as city-scale reconstruction [18], Structure-from-Motion (SfM) free 3D Gaussian Splatting [19], and 4D Gaussian Splatting, which includes the time domain [20].

### B. RF-3DGS

Inspired by the similarity of our problem and scene reconstruction using optical radiance field, we propose developing an approach to model the wireless channel through the Radio Radiance Field (RRF). However, we face the following three challenges: First, since the wireless channel fundamentally differs from photographs, how can we design a learnable RRF representation structure that effectively captures the multi-modal Spatial-CSI? Second, given a well-trained RRF representation, how can we efficiently query the received wireless channel at an arbitrary Rx location? Third, with a set of wireless samples, how can we use them to train the RRF representation to accurately model the wireless channel?

In this paper, we propose RF-3DGS, a method that addresses the aforementioned challenges and enables rapid, precise, site-specific reconstruction of the RRF from very sparse training inputs. Compared to previous works, RF-3DGS offers several advantages, including ultra-fast training and inference speeds, concise representation size, and the ability to reconstruct the Spatial-CSI of each MPC in the RRF reconstruction.

This enhanced RRF representation enables efficient spatial management of massive MIMO systems. Furthermore, the real-time inference and explicit geometric representation make it highly beneficial for other wireless system tasks, such as sensing and digital twin applications [21], [22], [23]. In addition, we explore various array signal processing techniques and propose a two-stage fusion training strategy to extract geometric information from visual input and integrate it into the RRF representation.

To demonstrate the performance of RF-3DGS, several test examples are presented in Fig. 1. Whether operating with the practical Minimum Variance Distortionless Response (MVDR) spectra generated by an  $8 \times 8$  patch antenna array or with ideal radio spatial spectra, which require more advanced and costly systems, RF-3DGS effectively reconstructs the radio radiance field in unvisited locations with very sparse input (only tens of samples in a complex environment). Moreover, RF-3DGS exhibits strong extrapolation capabilities thanks to the two-stage fusion training. The effectiveness of RF-3DGS is evident in Fig. 1, where our method significantly outperforms the State-of-The-Art (SOTA)  $NeRF^2$  [24].

Quantitatively, RF-3DGS achieves an 84.64% error reduction in reconstructed spatial spectra quality compared to  $NeRF^2$ . Meanwhile, RF-3DGS requires only 3 minutes for RF radiance field reconstruction and just 2 ms to render a spectrum at an arbitrary array position, whereas  $NeRF^2$  takes 3 hours of training and approximately 1 second to render a new spectrum.

To further evaluate its effectiveness in wireless communication, the synthesized spatial spectra are utilized to generate Conventional Beamforming (CBF) steering vectors. The results indicate that in the ideal spectrum scenario, RF-3DGS accurately guides the steering angle with a median deviation of  $5.94^\circ$  at the test points. Moreover, since RF-3DGS also

encodes additional CSI features, the reconstructed AoD and delay channel spectra exhibit high similarity to the ground truth. We also assessed our digital twin framework by comparing it with physical twin measurements, which demonstrate a high degree of consistency with the physical reality.

### C. Contributions

Our contributions are summarized as follows:

- First, we propose the fundamentals of the RRF method and theoretically analyze how the RRF can represent radio propagation, how to query the wireless channel from an RRF representation, and how to reconstruct the RRF from wireless samples.
- Next, we propose the RF-3DGS framework, which is characterized by two key features: (1) representing multi-modal Spatial-CSI using carefully designed CSI-encoded spherical harmonic (SH) functions, and (2) integrating visual and radio data into the RRF representation through a novel two-stage fusion training strategy to address the limitations of wireless samples.
- Lastly, we construct a digital twin framework comprising comprehensive real-world wireless measurements and precise radio spatial spectra simulations in its digital replica. We further demonstrate how our method benefits massive MIMO spatial management and advanced applications such as Integrated Sensing and Communications (ISAC).

## II. FUNDAMENTALS OF THE RRF METHOD

In this section, before detailing RF-3DGS, we first establish the theoretical foundations of the RRF method. We begin by defining the RRF representation structure, which models the radio propagation, followed by a discussion on how the wireless channel can be rendered from this representation. Lastly, we discuss training the RRF representation to accurately model the wireless channel.

### A. Overview of RRF Method

An RRF is generally defined as a model that describes how radio waves are emitted from every point in a 3D space toward the entire spherical domain (the full  $4\pi$  steradians), given a bounded environment  $\mathcal{E}$  and the  $\mathbf{x}$  configuration  $\mathcal{T}$ . A practical RRF representation,  $\mathcal{R}(\mathcal{E}, \mathcal{T}) = \{c(\mathbf{x}, \mathbf{d}), \alpha(\mathbf{x})\}$ , is composed of two components: 1) the RRF function  $c(\mathbf{x}, \mathbf{d})$ , where  $\mathbf{x} \in \mathbb{R}^3$  is the 3D coordinate and  $\mathbf{d}$  is the radiating direction; 2) the geometry of the environment, represented by a density field function  $\alpha(\mathbf{x})$ .

As shown in Fig. 2, the RRF function  $c(\mathbf{x}, \mathbf{d})$  describes the radio radiance field across the entire 3D space. For a specific point  $\mathbf{x}_r$ , the radio radiance  $c_{\mathbf{x}_r}(\mathbf{d})$  is a spherical function that describes the MPCs originating or retransmitting from this point at arbitrary direction  $\mathbf{d}$ . For a specific point  $\mathbf{x}_r$  and direction  $\mathbf{d}_r$ , they define the geometry of a ray in 3D space, and  $c_{\mathbf{x}_r, \mathbf{d}_r}$  represents the Spatial-CSI values of the MPC corresponding to this ray. Because this ray is actually the final segment of a complete radio propagation path from the Tx to a Rx on this ray, the path also corresponds to an MPC of

the wireless channel to the Rx. Thus, hereafter, we sometimes integrate the concepts of a ray and its corresponding MPC as ray (MPC) for simplicity.

For an Rx that lies on a ray (MPC), if the ray is within the Rx's Field of View (FoV) with no obstacles between the ray origin  $\mathbf{x}_r$  and the Rx, the Rx can receive this MPC. To handle the potential blockages, the geometry is required. This is represented by the density field function,  $\alpha(\mathbf{x})$ , which assigns zero to free space, low values to translucent objects, and high values to solid object surfaces (as reconstructing the interior of solid objects is both challenging and unnecessary).

Given a well-trained RRF representation  $\mathcal{R}$  and the current Rx configuration, the wireless channel between the Tx and Rx can be rendered as a radio spatial spectrum  $\mathcal{S}(\mathcal{R}, \mathcal{P}_{\text{Rx}}, \mathbf{x}_{\text{Rx}}, \mathbf{d}_{\text{Rx}})$ , where  $\mathbf{x}_{\text{Rx}}$  and  $\mathbf{d}_{\text{Rx}}$  are the position and direction of the Rx, and  $\mathcal{P}_{\text{Rx}}$  is the Rx projection model defined by the Rx array's FoV and the query requirements. This radio spatial spectrum enables efficient querying of Spatial-CSI for MPCs and facilitates high-level applications.

### B. Structure of the RRF Representation

For the RRF representation  $\mathcal{R} = \{c(\mathbf{x}, \mathbf{d}), \alpha(\mathbf{x})\}$ , although the RRF function  $c(\mathbf{x}, \mathbf{d})$  can describe the Spatial-CSI of the radio radiance originating from every 3D point  $\mathbf{x}$ , as shown in Fig. 2, the geometry is still necessary for two reasons. First, as mentioned, the subsequent rendering process requires the geometry to handle the blockages. Second, for efficiency, we only need to reconstruct and render the RRF function  $c(\mathbf{x}, \mathbf{d})$  for object points  $\mathbf{x}_{\text{obj}}$ , where  $\mathbf{x}_{\text{obj}} \in \{\mathbf{x} | \alpha(\mathbf{x}) \neq 0\}$ . These considerations arise because physical radio radiance is only actually emitted from radiance sources, such as the Tx and retransmitting surfaces depicted by the red dots in Fig. 2. In free space, the RRF function  $c(\mathbf{x}, \mathbf{d})$  is assigned with zero value, which should be distinguished from the EM field that spreads the whole space. The latter requires significantly more resources for simulating, reconstructing, and representing.

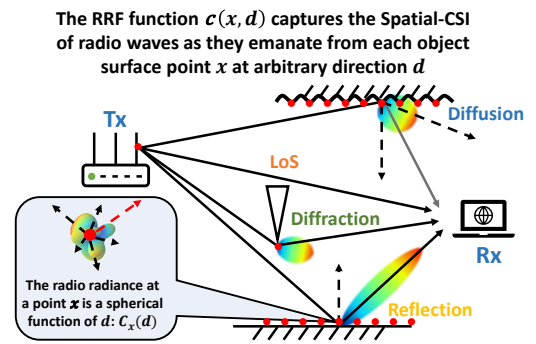


Fig. 2. Represent multi-path propagation of radio waves using the Radio Radiance Field.

More specifically, for a given ray (MPC) defined by its ray origin  $\mathbf{x}_r$  and direction  $\mathbf{d}_r$ , the Spatial-CSI values  $c_{\mathbf{x}_r, \mathbf{d}_r}$  of this ray (MPC) should include channel gain, delay, AoA, AoD, and polarization. However, in this work, we only encode the channel gain, delay, and AoD into  $c_{\mathbf{x}_r, \mathbf{d}_r}$ , as the AoA is already determined by the geometry of this ray and

the Rx direction, and the polarization will be considered in future work due to its challenges in field measurement and simulation. Therefore, a practical representation of the RRF is  $\mathcal{R} = \{\mathbf{c}(\mathbf{x}_{\text{obj}}, \mathbf{d}), \alpha(\mathbf{x})\}$ , which encompasses the geometry of the entire 3D space and the radio radiance at each object point.

### C. Rendering the RRF Representation

As mentioned earlier, the purpose of RRF method is rapid and accurate querying of the Spatial-CSI of wireless channel between a fixed Tx and an arbitrary Rx position.

To achieve this, given a well-trained RRF representation  $\mathcal{R}$ , the goal is to query how radiance arrives at a Rx position from different directions. As shown in the upper-left part of Fig. 3, a practical approach is to query the Spatial-CSI at a set of uniformly distributed AoAs (gray arrows) within the array's FoV (red spherical cap), assuming the presence of MPCs at each AoA, even though most queried AoAs may not exhibit strong MPCs. The queried Spatial-CSI values then form the radio spatial spectrum  $\mathcal{S}(\mathcal{R}, \mathcal{P}_{\text{Rx}}, \mathbf{x}_{\text{Rx}}, \mathbf{d}_{\text{Rx}})$ , which accurately depicts the wireless channel between the Tx and Rx. In particular, the projection model  $\mathcal{P}_{\text{Rx}}$  defines how the

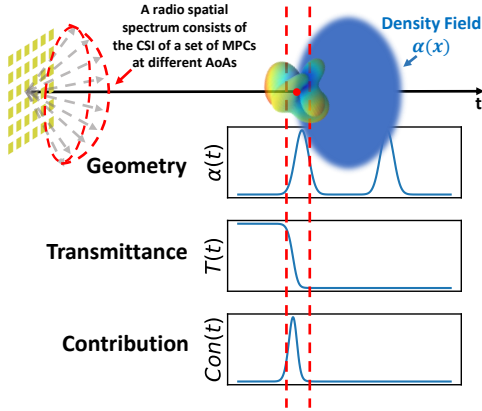


Fig. 3. Render a radio spatial spectrum from the RRF representation.

AoAs to be queried are distributed within the FoV and how the Spatial-CSI values are mapped to pixels in a 2D image, similar to an “RF picture”. These “RF pictures” have parallel channels corresponding to mentioned channel gain, delay, and AoD, much like RGB images, but require more careful processing. The design of the projection model  $\mathcal{P}_{\text{Rx}}$  is flexible. For better visualization, we use a simple pinhole camera model, consisting of a  $200 \times 300$  pixel grid with a horizontal FoV of  $90^\circ$ , as shown in Fig. 1. More efficient projection model will need to be investigated for future practical implementations.

For querying at each AoA, the alpha-blending rendering technique is applied. As shown in Fig. 3, given a AoA to be queried, we launch a rendering ray along this AoA. This rendering ray is represented as  $\mathbf{r}(t) = \mathbf{x}_{\text{Rx}} + t\mathbf{d}_{\text{ray}}$ , where the 3D position  $\mathbf{x}$  is simplified to a one-dimensional coordinate  $t$  on the ray for convenience.  $\mathbf{d}_{\text{ray}}$  is the direction of this rendering ray from the array central point  $\mathbf{x}_{\text{Rx}}$  to the red surface point. To render the received Spatial-CSI  $\mathbf{c}_{\text{recv}}$  (should

be distinguished from the RRF function), the alpha-blending rendering equation can be expressed as:

$$\mathbf{c}_{\text{recv}}(\mathbf{x}_{\text{Rx}}, \mathbf{d}_{\text{ray}}) = \int_{t_n}^{t_f} \mathbf{c}(t, \mathbf{d}_{\text{ray}}) \cdot T(t) \cdot \alpha(t) dt, \quad (1)$$

$$T(t) = \exp\left(-\int_{t_n}^t \alpha(s) ds\right), \quad (2)$$

where  $T(t)$  is the transmittance, representing the accumulated density from the image plane to  $t$ , with  $t_n$  and  $t_f$  being the pre-defined lower and upper integration limits along the ray. Notably, as shown by the three curves in the lower-right part of Fig. 3, when the rendering ray intersects the blue ball surface with high density  $\alpha(t)$ , the transmittance  $T(t)$  drops sharply from 1 to 0. As a result, the portion of the ray behind the intersection has little contribution,  $Con(t) = \alpha(t)T(t)$ , to the  $\mathbf{c}_{\text{recv}}$ . Similarly, the portion of the ray in free space before the intersection also contributes little due to their zero density. Thus, only the radio radiance of the first encountered surface point significantly influences the received Spatial-CSI, which aligns with our intuition.

### D. Reconstructing the RRF

To reconstruct the RRF  $\mathcal{R}$  from a set of training radio spatial spectra captured at different array poses, we first need a learnable representation capable of encoding the geometry  $\alpha(\mathbf{x})$  and the radio radiance  $\mathbf{c}(\mathbf{x}, \mathbf{d})$ , while maintaining differentiability to the two functions. Additionally, the representation should be editable, concise, and easy to initialize.

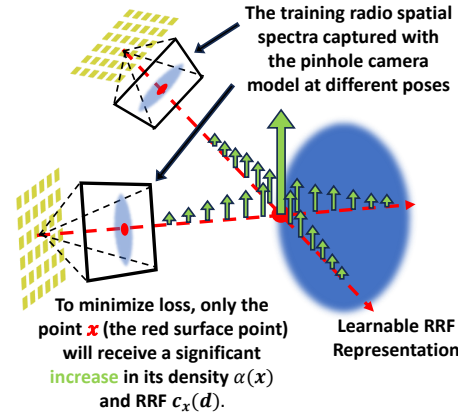


Fig. 4. Train a RRF representation from radio spatial spectra.

Now, assuming we have a well-initialized learnable RRF representation, this representation is iteratively optimized through gradient descent to minimize the loss between the rendered radio spatial spectra and the training spectra. While it is clear that the alpha-blending rendering equation is also differentiable to the two functions, allowing the loss and representation to be directly connected, the efficiency of this training process requires seamless cooperation between the representation structure, the rendering pipeline, and the training strategies. Thus, building on 3DGS, RF-3DGS addresses these challenges by utilizing explicit 3D Gaussian distributions



and SH Functions to represent the RRF  $\mathcal{R}$ . For rendering, a parallelized rasterization pipeline is employed, along with adaptive training strategies modified specifically for RRF reconstruction.

Beyond these techniques, the core philosophy behind how such methods capture the RRF  $\mathcal{R}$  is straightforward. As illustrated in Fig. 4, since the red surface point on the object appears in multiple training radio spatial spectra, each spectrum contains a rendering ray that renders this point during optimization. As all these rays converge at the actual position of the surface point in 3D space, during gradient descent, only this surface point in the representation should receive an increase in density and its corresponding Spatial-CSI, as this is the optimal solution to minimize the loss functions associated with those rays. This insight suggests that our radio spatial spectra should contain sufficient and accurate geometric information while maintaining consistency across different views. However, wireless samples naturally lack geometric information, and such requirements necessitates expensive measurement systems and significant processing effort. RF-3DGS overcomes this challenge with a two-stage fusion training strategy to efficiently integrate geometric information from visual inputs into the RRF reconstruction.

### III. RELATED WORKS

**Traditional Methods:** Radio propagation modeling has been extensively studied over the decades. Empirical models, such as the Okumura-Hata [25] and COST 231 models [4], are widely used for predicting approximate path loss in large-scale environments. Computational EM simulations [6], utilizing acceleration methods like the finite-difference time-domain (FDTD) method [7], offer high accuracy for applications such as antenna design [8] or near-field simulations [9]. While these methods are effective for specific tasks, they fall short in more general scenarios.

**Ray tracing:** Originally developed for computer graphics, ray tracing has long been adapted for radio propagation modeling [26], [27]. It models radio waves as rays to simulate complex RF interactions such as reflection, diffraction, and scattering [10], [11], [12]. Although ray tracing is suitable for a wide range of environments, it is limited by high computational complexity, stringent requirements for environmental information, and an inflexible pipeline that is difficult to calibrate.

**Neural Network Methods:** These methods use broader environmental information as input to generate outputs such as CSI [28], [29] or 2D path loss maps [30], [31]. Although these approaches are fast, provide acceptable accuracy, and perform well within the domain defined by the training data, they lack determinism and interpretability.

**Radiance Field Reconstruction Methods:** Since the success of radiance field reconstruction methods in CV, several works have extended these methods to the RF domain. We briefly introduce some of them here.

*NeRF*<sup>2</sup> reconstructs a “squared” radio radiance field that considers both “camera” and “light source” locations as inputs. However, its spectra, generated using CBF at 915 MHz with

linear scale transformation and per-view normalization, suffer from strong interference, inconsistencies across views, lack of geometric information, and distance-dependent decay, all of which conflict with the requirements discussed earlier. To maintain effectiveness, *NeRF*<sup>2</sup> requires a sample density 2000 times higher than in this work, negating the advantage of sparse sampling that NeRF offers. RayProNet [32] integrates environmental information as input and uses an explicit “light probe” as the radio radiance field voxel. However, RayProNet is limited to producing only 2D path loss maps, without offering more detailed information.

### IV. PROPOSED RF-3DGS FRAMEWORK

In the previous section (Sec. II-D), three critical challenges for efficient RRF reconstruction were identified. The first challenge is designing a learnable representation that can efficiently capture the geometry and the radio radiance of each object point. The second challenge involves developing an efficient rendering pipeline and training strategy to improve reconstruction speed and quality. The third challenge is the inherent lack of geometric information in radio spatial spectra. In the following subsections, we will introduce the representation structure, rendering pipeline, and training strategy of RF-3DGS, which are designed to address these three challenges.

#### A. 3D Gaussian Distributions

Unlike NeRF, which uses two neural networks to directly fit the density field function  $\alpha(\mathbf{x})$  and the RRF function  $\mathbf{c}(\mathbf{x}, \mathbf{d})$  for all continuous points  $\mathbf{x}$ , 3DGS utilizes millions of learnable 3D Gaussian distributions (hereafter referred to as “Gaussians”) as the geometry representation and only reconstructs the radiance for each Gaussian center. In RF-3DGS, we adopt a similar configuration, using Gaussians as the basic primitives for the geometry. Each Gaussian has its own learnable parameters, including the basic density  $\alpha_g$ , the center (mean) of the Gaussian  $\mathbf{x}$ , and the shape of the Gaussian, which is typically defined by a  $3 \times 3$  covariance matrix  $\Sigma$ . The density field of a single 3D Gaussian distribution can be represented as:

$$\alpha(\mathbf{x}) = \alpha_g \cdot e^{-\frac{1}{2}(\mathbf{x})^T \Sigma^{-1}(\mathbf{x})} \quad (3)$$

However, due to the fact that the covariance matrix of a Gaussian must be positive semi-definite, it cannot be directly constrained during gradient descent. Therefore, the shape of the 3D Gaussians is represented by a more constrained set of parameters. The covariance matrix can be decomposed as:

$$\Sigma = \mathbf{R} \mathbf{S} \mathbf{S}^T \mathbf{R}^T \quad (4)$$

where  $\mathbf{S}$  is a  $3 \times 3$  scaling diagonal matrix, and its diagonal elements consist of a 3D scaling vector  $\mathbf{s}_{scal}$  that controls how the 3D Gaussian spreads along the three dimensions. The matrix  $\mathbf{R}$  is a  $3 \times 3$  rotation matrix (an orthogonal matrix), which can be mapped with a quaternion  $\mathbf{q}$  that controls the rotation of the Gaussian, as shown in Fig. 5. Both  $\mathbf{s}_{scal}$  and  $\mathbf{q}$  are easier to constrain within valid domains. For instance, large, anomalous Gaussians with excessive  $\mathbf{s}_{scal}$  values can be excluded, and all  $\mathbf{q}$  values can be normalized to unit length, ensuring validity.

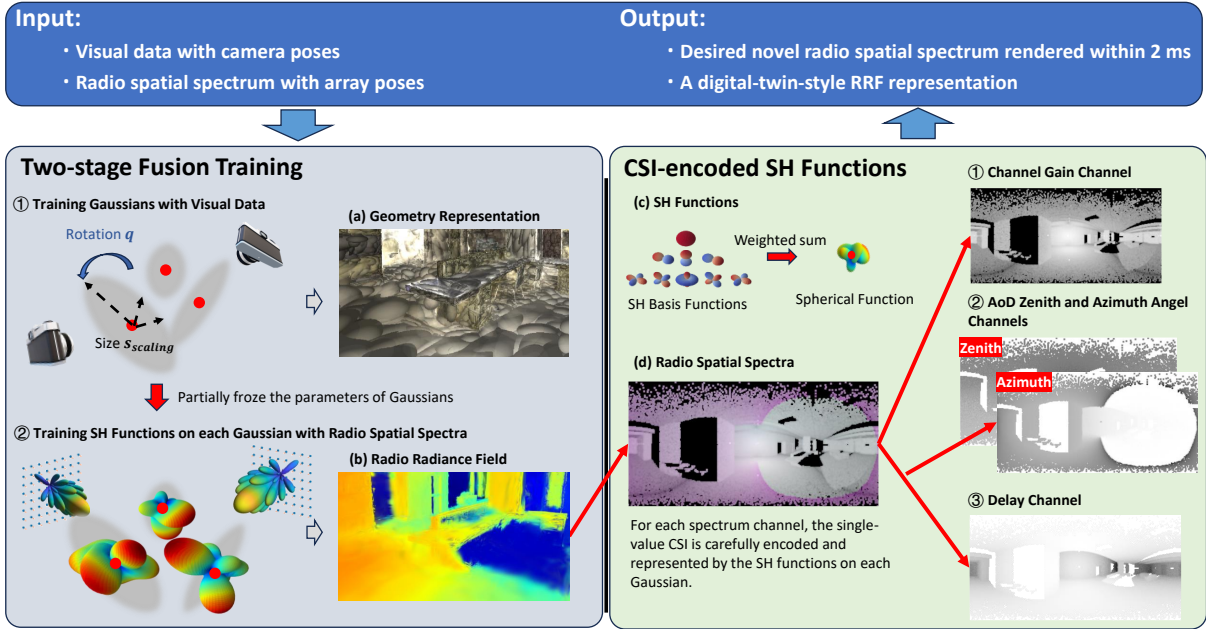


Fig. 5. RF-3DGS pipeline. (a) The extracted geometry representation from the visual data, consisting of millions of Gaussians, where the Gaussians are visualized by their contour surfaces. (b) The reconstructed radio radiance field, where the objects are illuminated by RF waves. (c) A demonstration of SH functions. (d) An example of the CSI-encoded spectrum and the corresponding decoded CSI spectra from the respective channels.

Thus, during the training process, the parameters of the millions of Gaussians are optimized, “moving” and “transforming” these Gaussians to precisely represent the geometry of the environment. This is illustrated in Fig. 5(a), where the Gaussians are visualized by their contours of distribution density at 0.8 (the value of  $e^{-\frac{1}{2}(\mathbf{x})^T \Sigma^{-1}(\mathbf{x})}$ ).

### B. CSI-encoded Spherical Harmonics Function

Given the explicit object geometry consisting of Gaussians with exact positions, we only need to reconstruct the radio radiance from each Gaussian center. For this purpose, we use SH functions rather than a neural network. As mentioned earlier, the radio radiance  $c_{\mathbf{x}}(\mathbf{d})$  at a point  $\mathbf{x}$  is a spherical function, and such a complex spherical function can be adaptively approximated by SH function, which is a linear combination of basis SH functions. This representation is illustrated in Fig. 5(c). The number of basis functions is determined by the degree; the higher the degree, the more basis functions are available, allowing for the representation of more complex spherical functions. For our purpose, a degree of 3 is sufficient for RRF reconstruction.

In the Sec. II-C, we showed the rendering of single-value radio spatial spectra and mentioned that multi-modal Spatial-CSI requires more careful processing. This is mainly because, unlike the RGB values in normal images that already have the same distribution, the channel gain, delay, and AoD of an MPC have very different forms. First, the channel gain represents the ratio between transmitted power and received power for this MPC, and also indicates its importance. Therefore, the channel gain serves as the basis to encode the other CSI values so that our RRF representation can capture more details of the important MPCs.

However, directly using the absolute value of the channel gain as the pixel value introduces a significant issue. For EM wave propagation in free space, the channel gain (path loss) follows the well-known Friis equation:

$$P_r = P_t \frac{G_t G_r \lambda^2}{(4\pi d)^2}, \quad (5)$$

where  $d$  is the distance between the Tx and Rx. This equation indicates that the received power decreases proportionally to  $1/d^2$ . Referring back to Fig. 3 and Eq. (1), we note that along a ray, the rendered channel gain is independent of the distance between the object surface point and the array. This discrepancy arises because the radiance field method was originally designed to mimic visible light behavior. For visible light, when viewing an LED bulb from 1 meter and then 2 meters away, the perceived brightness does not drop by four times. This is explained by the human eye’s response to light intensity, which follows a logarithmic-like curve and spans a dynamic range of approximately 100 dB [33]. Therefore, the distance-dependent intensity decrease usually only results in a 1-2 dB drop in brightness, which is negligible. Consequently, in this paper, we convert the channel gain spectrum to the dB scale to mimic such distance-independent decay. Notably, this lossy transformation is not a compromise of the radiance field method’s limitations, but rather a way to take advantage of the visual intensity range. This transformation allows the spectrum to capture more details of the RRF, as shown in Fig. 8, where the dB scale spectrum more clearly describes the radio radiance field, at the cost of a few dB deviation in reconstruction.

Next, the dB-scaled channel gains are mapped to pixel values in the range [0, 255]. The upper limit of the channel gain is set to the free space propagation loss at 0.5 meters to

avoid unexpected high values in testing and online operation. The lower limit is the lowest sampled value in the training samples, usually the noise level. For improved visualization, most demonstrations in this paper apply a “jet” colormap to single-channel radio spatial spectra.

Thus, along with the channel gain spectrum, the AoD and delay can be encoded using parallel channels. Specifically, AoD can be perfectly represented by our current RRF representation, as it only depends on the geometry of each ray. Therefore, we decompose it into two channels: one encoding the azimuth angle ( $0^\circ$  to  $360^\circ$ ) and the other encoding the zenith angle ( $0^\circ$  to  $180^\circ$ ). These two angles of a MPC (pixel) then, which reflect the importance of this MPC.

For the delay channel, we currently define “delay” as the normalized delay of each MPC relative to the first-arrival MPC, ranging from 0 to 200 ns. MPCs exceeding 200 ns are discarded considering the indoor environment in this study. Although time of flight (ToF) would be preferable, it is difficult to acquire in field measurements, and it cannot be represented in the current RRF representation, as it is linearly related to the radio travel distance. The normalized delay alleviates this issue. For example, considering different Rx positions along a ray corresponding to the first-arrival MPC, the delay of later MPCs from other directions will slowly vary, which can be perfectly captured by the current RRF representation. However, once the different Rx positions are along a ray that does not correspond to the first-arrival MPC, the delays of other MPCs may deviate from the true delay. The larger the angle between the first-arrival MPC ray and the rays corresponding to later MPCs, the larger the deviations will be. However, such delay deviations are not significant, as shown in our later test of reconstructing delay spectra at unvisited locations.

Furthermore, the deviation in channel gain due to the dB scale and the deviation of delay representation can be further addressed with more in-depth development of the representation structure and rendering pipeline, which will be explored in future work.

### C. Rendering RRF with the 3DGS Rasterization Pipeline

As the millions of 3D Gaussians collectively define a density field function, and the SH functions define the radio radiance of discrete object points (the means of the Gaussians), the alpha-blending rendering can be directly applied to the Gaussians along each ray, without relying on complex and lossy sampling strategies. However, as there are thousands of pixels in a spectrum, the rendering process must be parallelized to improve efficiency. Thus, instead of rendering the rays one by one which query all the Gaussians for each ray, each Gaussian is “splatted” onto the image plane, and all affected pixels are rendered simultaneously.

Specifically, for each individual Gaussian, the splatting is traditionally defined by the view transform matrix  $\mathbf{W}$  and the perspective projection matrix  $\mathbf{P}$ . However, to simplify the calculation and increase stability, the Jacobian affine approxi-

mation  $\mathbf{J}$  of the perspective projection is used to splat the 3D Gaussian onto the image plane, as given by:

$$\Sigma' = \mathbf{J}\mathbf{W}\Sigma\mathbf{W}^T\mathbf{J}^T, \quad (6)$$

where  $\Sigma'$  is the covariance matrix of the projected 2D Gaussian. This affine approximation can be interpreted as each 3D Gaussian being first flattened to a 2D Gaussian by orthogonal projection along the camera depth axis, meaning that parts of the Gaussian do not appear larger as they get closer or smaller as they move further away, which is the cost of the affine approximation. Then, the 2D Gaussians are normally projected onto the 2D plane, following the perspective projection principle.

Next, an efficient rasterization rendering pipeline, well-suited for GPU computational structures, is employed. First, given the current rendering image plane and view frustum, the image plane is divided into  $16 \times 16$  tiles, and the view frustum is divided accordingly. For each tile, only the Gaussians within the corresponding divided view frustum are selected (following a specific criterion) and sorted based on their depth to the plane. Finally, the computation within each tile consists of parallelized threads rendering the sorted Gaussians onto each pixel. Once a pixel is saturated with little transmittance, meaning that further Gaussians cannot affect this pixel, the thread rendering this pixel is terminated. Further details about the sorting process and GPU memory management for the millions of Gaussians can be found in [17].

### D. Two-Stage Fusion Training

Given the rendered spectra from the learnable RRF representation and the training spectra, the loss function used in this work is a combined loss function. This function is defined as the  $L1$  loss plus a differential Structural Similarity Index Measure (D-SSIM) term:

$$\mathcal{L} = (1 - \lambda)\mathcal{L}_1 + \lambda\mathcal{L}_{D-SSIM}, \quad (7)$$

where  $\lambda$  is a predefined parameter, set to 0.2 in this work. The gradient descent then backpropagates this loss through the differentiable rasterization pipeline to the learnable parameters of each Gaussian.

However, as mentioned earlier, a major challenge is that the radio spatial spectrum naturally lacks geometric information. From Fig. 8, even the ideal spectrum can only be considered a low-quality “photo”, with other spectra offering even less geometric detail. In RF-3DGS, we assume access to the radio spatial spectra and the visual data, which serve as a low-cost supplement to geometric information. The proposed two-stage fusion training process is designed to extract geometric information from the visual data to enhance the RRF representation.

Before the training begins, if the visual data consists of photos or video without camera intrinsic and extrinsic parameters, an initialization process is required to estimate these parameters and generate initial point clouds using SfM. Otherwise, this process can be skipped, allowing training to start from random point clouds.

Once initialization is complete, the first stage of training begins with a warm-up phase. During this phase, the Gaussians

are trained using resolution-reduced images, enabling them to quickly capture global geometry rather than getting stuck on optimizing fine details. The image resolution is doubled twice, after 250 iterations and 500 iterations, until the original resolution is reached.

Following the warm-up, a periodic densification process refines the Gaussians every 100 iterations. In regions where the number of Gaussians is insufficient to represent intricate 3D geometry, the densification process splits large Gaussians and clones small Gaussians to create more learnable “ellipsoids” in those regions. Gaussians with very small density values or those with excessively large footprints in the views are removed to prevent the “floater” artifact problem, a common issue in radiance field reconstruction methods.

To manage the quantity of Gaussians, their basic density values  $\alpha_g$  are reset towards zero every 3000 iterations. This reset allows key Gaussians to quickly regain their original density values during optimization, while abnormal or unnecessary Gaussians, whose density values increase slowly, are removed in subsequent densification steps.

After establishing a well-trained geometry representation, the second stage begins. In this stage, RF-3DGS uses the collected radio spatial spectra to train the CSI-encoded SH functions and the basic density of each Gaussian, while freezing the positions  $\mathbf{x}$ , rotation  $\mathbf{q}$ , and scaling  $\mathbf{s}_{scal}$ . This setup ensures that the geometry representation has the adaptive capability to handle inconsistencies between the visual and radio geometries (since certain materials may appear opaque in visual data but translucent under radio waves). After optimization, the new CSI-encoded SH functions can be interpreted as the objects being re-illuminated by the given Tx radio, with multiple channels corresponding to different Spatial-CSI properties.

The advantage of the proposed two-stage fusion training is not only that it requires low-cost visual data as a supplement, but also that it exhibits extrapolation capabilities, as shown in Fig. 6. This capability arises from the accurate visual geometric information, which provides the actual radiance source location, allowing vague or interfered radio spectra to be mapped to the correct locations rather than being assigned to vague floaters, as seen in *NeRF*<sup>2</sup>.

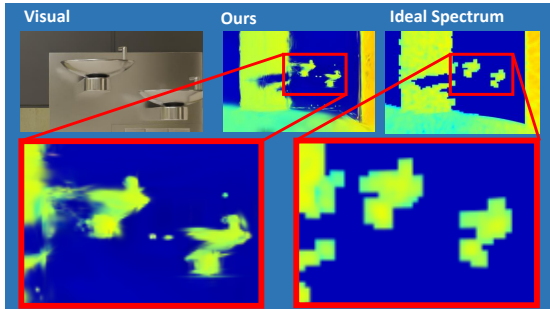


Fig. 6. Extrapolation ability of the proposed two-stage fusion training. Both spectra are rendered using the same pinhole camera model. The ideal spectrum, serving as the training target, is limited by the maximum number of MPCs our RTX A6000 48 GB GPU can handle and the minimum array pattern lobe width needed for spectrum continuity.

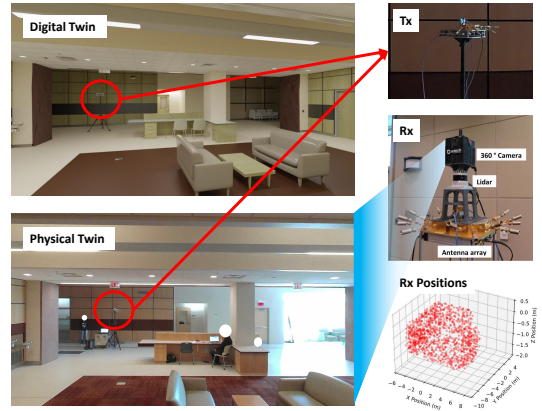


Fig. 7. Dataset overview. Our dataset consists of field measurements provided by NIST [34], along with a simulated digital replica conducted under the same configuration and environmental conditions.

### E. Generating Radio Spatial Spectrum

Although RF-3DGS has largely addressed the challenges of RRF reconstruction, obtaining high-quality radio spatial spectra remains crucial. Considering applications in the wireless communication domain, we assume the system employs a common wireless communication configuration, typically involving half-wavelength spaced Uniform Planar Arrays (UPAs) operating with either a digital beamformer or a fully analog beamformer to generate baseband digital signals. Systems specifically designed for RF imaging/radar are not considered in this paper.

In this work, we constructed a digital twin framework to evaluate the effectiveness of RF-3DGS, comprising comprehensive field measurements in a 14 m × 15 m lobby and a digital replica of the same space with a full radio simulation pipeline, as shown in Fig. 7. The 60 GHz measurement data [34] was provided by the National Institute of Standards and Technology (NIST), USA. The simulator used is Sionna [35], an open-source communication simulator developed by NVIDIA, which is equipped with the Sionna RT [36] ray tracer and supports GPU acceleration.

As illustrated in Fig. 8, our simulation environment is a precise 3D replica of the NIST lobby with the same Tx position. First, the digital twin of the environment is reconstructed using photographs and LiDAR data. More specifically, each object is carefully segmented by material, and each material is assigned the corresponding EM properties. These EM models are then imported to the simulator, which uses ray tracing to simulate radio propagation paths. For the fixed Tx position, the radio propagation paths are captured at a set of sparse random Rx positions distributed throughout the lobby. Since the setup simulates a fully diffuse environment at 60 GHz, the number of paths between each Tx-Rx pair often exceeds 300,000, which limits a UPA array size to 8×8. Next, the simulated MPCs, distributed in the angle domain (shown in Fig. 8), are received by the UPA. Finally, the received signals at each element are processed using various Array Signal Processing (ASP) techniques to generate the desired radio spatial spectrum. Further details on the simulation configuration and data processing are available in our open-source code.



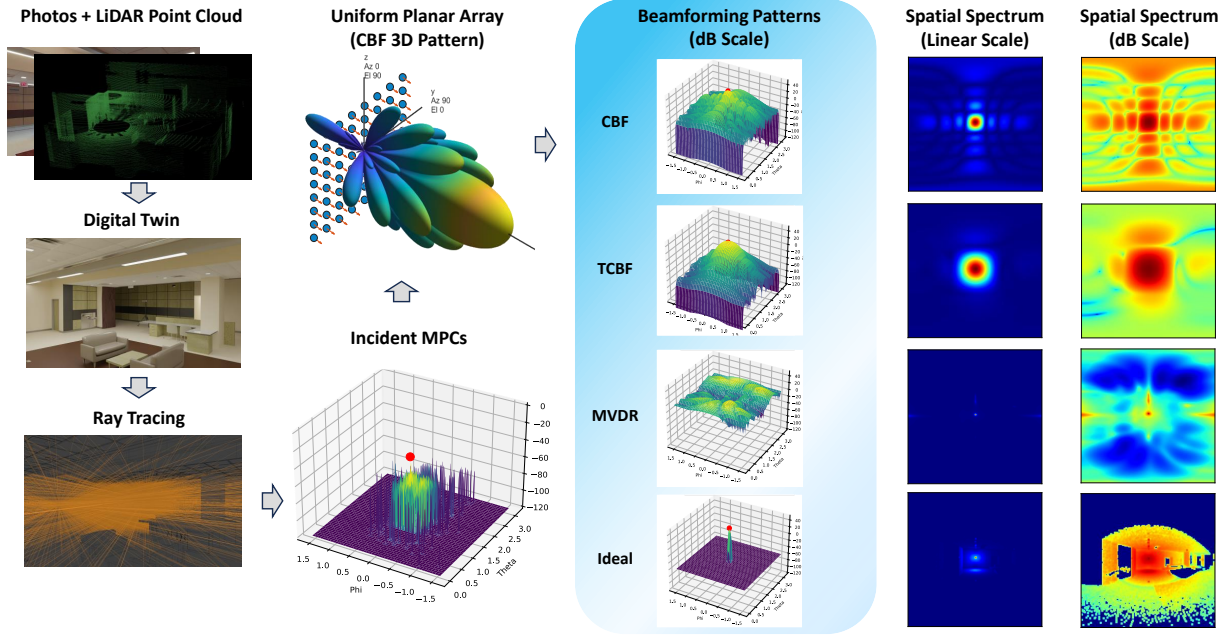


Fig. 8. Full radio simulation pipeline with various beamforming patterns and their corresponding spectra.

Before introducing the ASP techniques, let's provide a brief scenario description. In a typical ASP scenario [37],  $M$  signals incident from different directions onto the array are received by the  $N$  elements of the UPA. These signals are processed by  $L$  steering vectors, resulting in the processed signals  $\mathbf{y}(t)$  across the  $L$  scanning directions. This process can be expressed as:

$$\mathbf{y}(t) = \mathbf{W}^H \cdot \mathbf{A}(\Theta, \Phi) \cdot \mathbf{s}_{\text{signal}}(t) + \mathbf{n}(t). \quad (8)$$

The signal vector  $\mathbf{s}_{\text{signal}}(t)$  is defined as:

$$\mathbf{s}_{\text{signal}}(t) = [s_1(t), s_2(t), \dots, s_M(t)]^T, \quad (9)$$

where  $s_m(t)$  represents the  $m$ -th incident signal characterized by its incident zenith angle  $\theta_m$  and azimuth angle  $\phi_m$ .  $\mathbf{n}(t)$  is the additive white Gaussian noise. The matrix  $\mathbf{A}(\Theta, \Phi)$  is a complex matrix of size  $N \times M$ , with each column corresponding to the array manifold vector of the  $m$ -th signal:

$$\mathbf{A}(\Theta, \Phi) = [\mathbf{a}(\theta_1, \phi_1), \mathbf{a}(\theta_2, \phi_2), \dots, \mathbf{a}(\theta_M, \phi_M)], \quad (10)$$

where each array manifold vector  $\mathbf{a}(\theta, \phi)$  is the product of the antenna pattern gain  $G(\theta, \phi)$  and the phase differences caused by the path differences  $\mathbf{d}(\theta, \phi)$  between each element and a reference location:

$$\mathbf{a}(\theta, \phi) = G(\theta, \phi) \cdot e^{-j \frac{2\pi \mathbf{d}(\theta, \phi)}{\lambda}}. \quad (11)$$

The objective in our case is to find an appropriate steering vector set  $\mathbf{W}^H = [\mathbf{w}_1, \mathbf{w}_2, \dots, \mathbf{w}_L]$ , that maximize the Signal-to-Interference-plus-Noise Ratio (SINR) of the signals in each corresponding AoA direction. As we mentioned in Sec. II-C, we use a pinhole camera model to generate the radio spatial spectrum, which means we need to scan the AoAs of all the  $200 \times 300$  pixels.

To accommodate different wireless systems, we explored various ASP techniques to provide an overview of spectra

that different systems can generate, as shown in Fig. 8, more specific, the CBF, TCBF and MVDR patterns and spectra are simulated by a  $8 \times 8$  UPA, the ideal spectra are generated by a synthesized ideal pattern with main lobe width  $3^\circ$ , which is close to the pattern of a  $64 \times 64$  UPA with CBF.

**CBF**, also known as the Bartlett beamformer [38], is a delay-and-sum beamforming technique. It adjusts the phase shifts of each array element to align their wavefronts in the desired scanning direction  $(\theta_l, \phi_l)$ . The CBF steering vector only compensates for phase differences, expressed as:

$$\mathbf{w}_{\text{CBF}}(\theta_l, \phi_l) = \frac{\mathbf{a}(\theta_l, \phi_l)}{\|\mathbf{a}(\theta_l, \phi_l)\|}. \quad (12)$$

Therefore, CBF requires only an analog beamforming system with phase shifters and a single RF chain. Fig. 8 illustrates the CBF pattern, which acts as a kernel convolved with incoming MPCs to form the spatial spectrum. This kernel exhibits numerous strong side lobes, leading to significant interference in the spectrum, even when represented on a linear scale. Furthermore, this kernel varies with different steering angles, complicating frequency-domain deconvolution for interference reduction [39].

To address this issue, we tested the CBF spectrum tapered by a Hann window [37] and found that while side lobe levels were suppressed, interference remained problematic on the dB scale.

**MVDR**, also known as the Capon beamformer [40], is a popular array signal processing technique characterized by its adaptive ability to maximize the SINR. Unlike CBF, which merely maximizes gain in the current scanning direction, MVDR optimizes the steering vector  $\mathbf{w}$  by solving the following problem:

$$\min_{\mathbf{w}} \mathbf{w}^H \mathbf{R} \mathbf{w} \quad \text{subject to} \quad \mathbf{w}^H \mathbf{a}(\theta_l, \phi_l) = 1, \quad (13)$$

where  $\mathbf{R}$  is the signal autocorrelation matrix. The optimal steering vector and the corresponding power spectrum can be written as:

$$\mathbf{w}_{\text{opt}} = \frac{\mathbf{R}^{-1}\mathbf{a}(\theta_l, \phi_l)}{\mathbf{a}^H(\theta_l, \phi_l)\mathbf{R}^{-1}\mathbf{a}(\theta_l, \phi_l)}, \quad (14)$$

$$P_{\text{MVDR}}(C) = \frac{1}{\mathbf{a}^H(\theta_l, \phi_l)\mathbf{R}^{-1}\mathbf{a}(\theta_l, \phi_l)}. \quad (15)$$

As shown in Fig. 8, the MVDR spectrum in both linear and dB scales has much higher resolution and significantly reduced interference, revealing some geometric structure of the scene. However, MVDR has two key limitations: it requires individual element responses, needing a full digital beamforming system, and it is sensitive to signal distortion due to its reliance on the autocorrelation matrix  $\mathbf{R}$ .

**Space Alternating Generalized Expectation maximization (SAGE)** algorithm [41] is an iterative technique for parameter estimation, particularly effective in array signal processing [42], [43]. Therefore, in our study, SAGE was used exclusively for extracting MPCs from field measurements, and the extracted MPCs were subsequently used to generate the spectrum. As shown in Fig. 14(b), the SAGE spectrum is generated by an equirectangular camera model and overlaid with a picture from a similar optical camera at same pose.

## V. EXPERIMENTAL RESULT AND EVALUATION

In this section, to evaluate the performance of RF-3DGS, we designed several experiments. First, we directly compared the performance of RRF reconstruction with other methods. Next, to assess its generalizability, we tested how different types of spectra affect the performance of RF-3DGS. To evaluate RF-3DGS’s effectiveness in massive MIMO spatial management, we conducted experiments to test its ability to predict the CBF steering vector. Finally, as mentioned, RF-3DGS reconstructs multi-dimensional CSI, and we tested the accuracy of the reconstructed AoD and delay.

### Performance of Radio Radiance Field Reconstruction:

In this part, we focus on evaluating the radiance field reconstruction performance. The dataset, consisting of 800 samples, splits into fixed 160 test samples and 640 training samples. Furthermore, the training samples were randomly selected in proportions of 20%, 40%, 60%, 80%, and 100%.

A important point is that only high-level metrics, such as LPIPS (lower is better), can effectively evaluate our spectra quality when compared to the ground truth. Traditional statistical metrics, such as the Peak Signal-to-Noise Ratio (PSNR) and SSIM, fall short. This issue has been widely discussed in the CV domain [44], [45]. As illustrated in Fig. 9, even though the spectrum predicted by our method is visibly of higher quality, the PSNR and SSIM yield similar values for both spectra, while only LPIPS reflects the difference accurately.

The main reason for this metric failure is that our scenario differs significantly from other visual task comparisons. In typical visual tasks, like evaluating compression or super-resolution, outputs are usually close to the perfect ground truth images, resulting in high metric scores (PSNR > 35

dB, SSIM > 0.9, LPIPS < 0.05), where errors are mostly pixel-wise.

In contrast, in our tasks, the reconstruction performance is considerably worse, with PSNR around 15 dB, SSIM around 0.5, and LPIPS around 0.4, and the ground truth also contains distortions and noise. These factors reduce the metric discriminative power, as critical errors, such as the loss of geometric structure, are obscured by less significant noisy errors. This issue is particularly severe for PSNR and SSIM, which heavily rely on statistical features, unlike LPIPS, which utilizes convolutional neural networks to extract “deep” features for similarity evaluation.

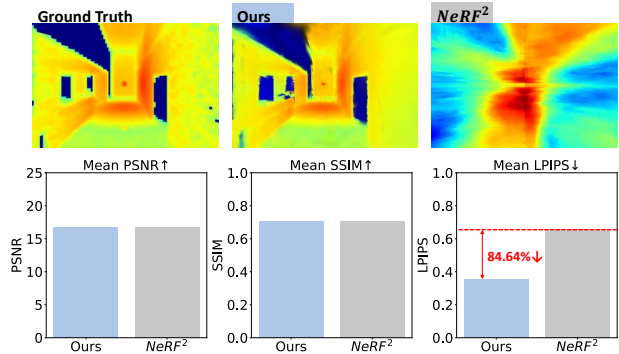


Fig. 9. Limitation of Statistical Metrics.

With LPIPS as the primary metric, we compared our method, RF-3DGS, with the Conditional GAN (CGAN) [46], representing black-box neural network approaches, and the SOTA  $NeRF^2$ . The results are presented in Fig. 10.

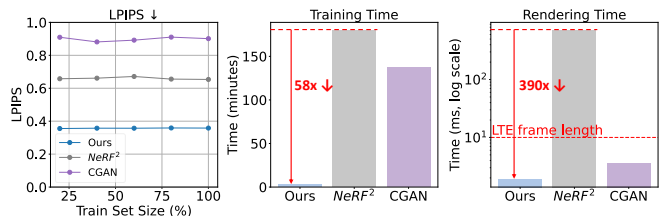


Fig. 10. General comparison.

RF-3DGS demonstrates significantly better LPIPS scores, requires orders of magnitude shorter training times, and offers rendering speeds faster than Long Term Evolution (LTE) frame rates. Additionally, RF-3DGS achieves high reconstruction quality with very sparse training samples, with rendering quality substantially degrading only when the sample count drops below approximately 20, depending on the uniformity of the sample distribution. For evaluating other parameters, we utilized the full training set to analyze their impact.

In contrast,  $NeRF^2$  struggles to capture detailed scene information, resulting in degraded LPIPS performance. As illustrated in Fig. 9,  $NeRF^2$  can only reconstruct large, illuminated floaters with limited details. Moreover, its training process takes approximately 3 hours, with each rendering requiring around one second.

For CGAN, the generator synthesizes images while the discriminator evaluates their fidelity, guiding the generator’s

optimization. The challenge lies in our sparse training input, where test inputs differ significantly from the training data. Consequently, the generator struggles to learn the mapping between Rx poses and target images, and the discriminator fails to provide useful gradients, resulting in poor overall performance.

**Impacts of Different Spectra:** To further evaluate the effects of different types of spectra, we trained RF-3DGS using CBF, TCBF, and MVDR spectra, testing them against both their corresponding homogeneous ground truth and the ideal spectrum ground truth. These two tests serve distinct purposes: first, homogeneous spectrum testing evaluates how spectra interference and inconsistency impact RF-3DGS’s reconstruction ability; second, ground truth testing assesses how these spectra degrade reconstruction quality. Fig. 11 provides a detailed comparison.

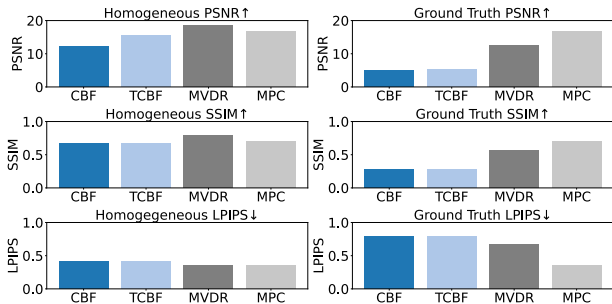


Fig. 11. Impacts of different spectra.

From the comparison, it is clear that the CBF and TCBF spectra impair both reconstruction ability and quality, evident from their poor performance across all metrics. The degradation in reconstruction quality is even more pronounced, with PSNR dropping to 5 dB. This suggests that for CBF and TCBF spectra, strong interference, and lack of geometric information severely limit the effectiveness of radiance field reconstruction in large environments.

In contrast, the MVDR spectrum group exhibits much higher performance than CBF and TCBF in both testing scenarios. More interestingly, in homogeneous spectrum testing, the MVDR spectrum group even results in higher PSNR and SSIM compared to the ideal spectrum group, which may appear counter-intuitive given the ideal spectrum’s higher quality and lower interference. However, as shown in Fig. 6, our method has an extrapolation ability that provides more details than the ideal spectrum. This extrapolation results in lower performance in statistical metrics like PSNR and SSIM but yields similar evaluations from LPIPS, further validating the effectiveness of the LPIPS metric in our tasks.

In summary, these comparisons demonstrate that RF-3DGS achieves significantly higher radio radiance field reconstruction quality, faster training speed, and faster rendering speed compared to other methods. Additionally, RF-3DGS requires only tens of samples to reconstruct the radiance field across a large lobby while providing an explicit geometric representation. These features and high performance underscore the potential of RF-3DGS in future 6G network applications.

**Application in MIMO Spatial Management:** To evaluate the effectiveness of RF-3DGS in wireless communication, we consider an application scenario where the Rx-side channel gain spectra are used to guide the Rx array in performing angle-domain CBF for signal reception. In this context, the AoA of the maximum-gain path is primary concern. The following results illustrate the angle deviation of RF-3DGS with different types of spectra. As shown in Fig. 12, although the CBF and TCBF spectra fail to accurately represent the scene geometry, they can still support simple beamforming tasks, though with some performance loss.

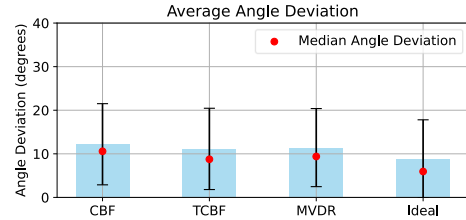


Fig. 12. Angle deviation of CBF guided by spectra.

**Spatial-CSI Prediction:** Another key feature of RF-3DGS is its capability to encode Spatial-CSI. In this paper, we tested its capability to represent the AoD and delay, which are critical in wireless communication.

As shown in Fig. 13, the results indicate the ability of RF-3DGS to reconstruct Rx-side AoD spectra and delay spectra. We also present examples of the decoded CSI spectra in Fig. 5. For the delay channel, the example demonstrates that the delay increases from the near reflection point to the far end, similar to a depth image. In the AoD-azimuth channel, although the angles vary according to physical laws, a sharp edge corresponding to the transition between 0 and 360° is visible. A more appropriate approach would involve using a 3D unit vector to represent such AoD information; however, in this paper, we use these two angles for a more intuitive demonstration.

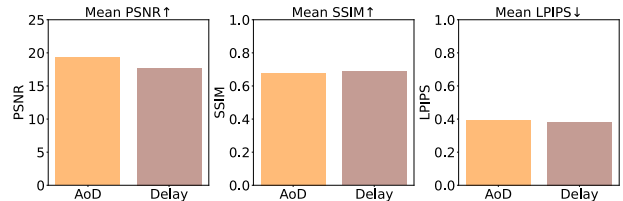


Fig. 13. Accuracy of encoded CSI spectra.

## VI. FIELD STUDY: A DIGITAL RADIO TWIN

In previous experiments, our testing relied on simulation datasets, which raised concerns about potential discrepancies between our digital twin and its physical counterpart. In this section, we demonstrate the fidelity of our digital radio twin framework, which includes both environment geometry and a comprehensive radio radiance field, and highlight its support for advanced applications like ISAC.

**Calibrating Radiance Field:** To validate the fidelity of our generated spectra, we first overlay them with equirectangular photographs taken from the same positions. The results show



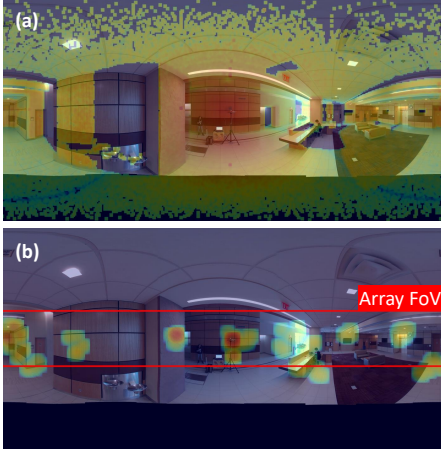


Fig. 14. (a) digital twin and (b) physical twin measurements comparisons [34].

that most spectra align well with the visual geometry, as illustrated in Fig. 14.

We also conducted field measurements at the same Rx locations using a synchronized Tx-Rx system, as depicted in Fig. 7. This system generates high-definition, precise Channel Impulse Response (CIR) between each Tx and Rx array element pair, which are processed by the SAGE algorithm to estimate key MPCs, including path loss, delay, AoD, and AoA. More details about this system are available in [43], [34]. Using these MPCs, we generated an MPC spectrum similar to our ideal spectra, as shown in the lower image of Fig. 14, which was then used to validate and calibrate our digital twin.

Two limitations in the field measurement process affect direct validation performance: the limited Rx vertical FoV, indicated by the red lines in Fig. 14 which also applies to Tx, and the system’s reliance on SAGE algorithms, which only estimate dominant MPCs. Consequently, the spectrum contains little information beyond several discrete MPCs.

This scenario is common when real systems have imperfections. In these cases, the advantages of RF-3DGS, such as rapid training and extrapolation ability, become particularly valuable. With just 3 minutes of re-training, we can produce a validated radio radiance field representation with high testing metrics, as shown in Fig. 15.

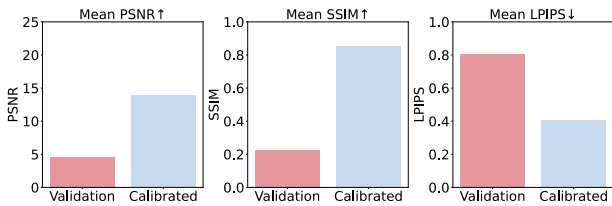


Fig. 15. Calibration with field measurement.

**An ISAC Scenario Demo with Digital Radio Twin:** Considering RF-3DGS’s exceptional ability to reconstruct the radio radiance field and model the environment with real-time wireless communication feedback, its potential for ISAC applications [21] is evident. Fig. 16 illustrates an ISAC scenario within digital radio twin, which consists of a normal digital twin framework and a well-trained RF-3DGS representation. On the left of Fig. 16, the ability of RF-3DGS to provide

real-time radio spatial spectra at arbitrary positions serves as prior knowledge of the radio scattering background. When a sensing target enters the scene as shown on the right of Fig. 16, optical monitors detect the target’s entry. However, visual data alone can only provide vague information about the target, limiting its utility for precise sensing. Such vague information can be used by the digital twin to notice the connected Rxs the relative location of the sensing target within their FoV, as highlighted by the red boxes. With both the real-time radio scattering background and the target’s potential direction, wireless communication feedback can be processed more effectively to extract detailed information about the sensing target. In comparison, traditional methods often struggle to distinguish and render such dynamic changes from wireless communication feedback in real time[47], [48].

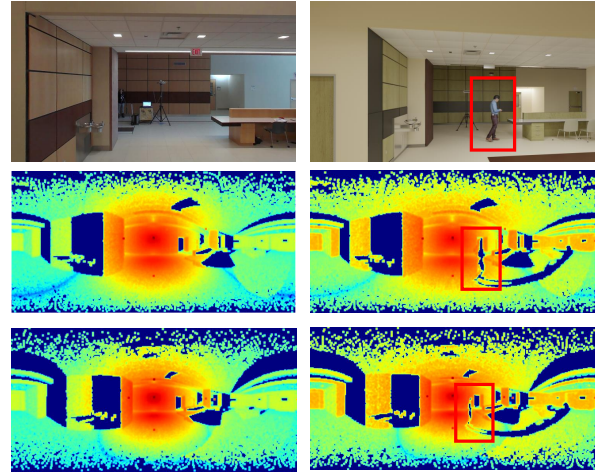


Fig. 16. ISAC scenario demonstration.

This capability is particularly advantageous in scenarios where timely and accurate sensing is critical, such as safety monitoring or automated navigation systems. RF-3DGS facilitates the simultaneous acquisition of communication signals and the precise reconstruction of the surrounding environment’s geometry in an explicit and efficient manner.

## VII. CONCLUSIONS

In this paper, we proposed RF-3DGS, a fast and efficient radio radiance field reconstruction method that demonstrates high performance in reconstruction quality. RF-3DGS significantly reduces the training time to just a few minutes, requires only 2 ms to render a spectrum, and needs only tens of samples to reconstruct a scene while providing an explicit geometry representation. We also showcased several applications of RF-3DGS and introduced a digital twin framework to validate and enhance the reconstruction process.

However, several challenges persist. A primary issue is the difficulty in obtaining accurate radio spatial spectra. Additionally, mitigating the deviation in the RRF representation demands further efforts to design novel representation structures and rendering pipelines. Furthermore, exploring more practical applications to fully leverage the benefits of RF-3DGS in 6G networks, particularly in areas such as cell-free massive MIMO and ISAC, remains a crucial avenue for future research.



## REFERENCES

- [1] R. W. Heath, N. Gonzalez-Prelcic, S. Rangan, W. Roh, and A. M. Sayeed, "An overview of signal processing techniques for millimeter wave MIMO systems," *IEEE journal of selected topics in signal processing*, vol. 10, no. 3, pp. 436–453, 2016.
- [2] M. A. Albreem, A. H. Al Habbash, A. M. Abu-Hudrouss, and S. S. Ikki, "Overview of precoding techniques for massive MIMO," *IEEE Access*, vol. 9, pp. 60764–60801, 2021.
- [3] L. Zhang, H. Sun, Y. Zeng, and R. Q. Hu, "Spatial Channel State Information Prediction With Generative AI: Toward Holographic Communication and Digital Radio Twin," *IEEE Network*, vol. 38, no. 5, pp. 93–101, 2024.
- [4] Y. Singh, "Comparison of okumura, hata and cost-231 models on the basis of path loss and signal strength," *International journal of computer applications*, vol. 59, no. 11, 2012.
- [5] P. Series, "Propagation data and prediction methods for the planning of indoor radiocommunication systems and radio local area networks in the frequency range 900 MHz to 100 GHz," *Recommendation ITU-R*, pp. 1238–7, 2012.
- [6] A. Bondeson, T. Rylander, and P. Ingelström, *Computational electromagnetics*. Springer, 2012.
- [7] D. M. Sullivan, *Electromagnetic simulation using the FDTD method*. John Wiley & Sons, 2013.
- [8] A. Hoorfar and V. Jamnejad, "Electromagnetic modeling and analysis of wireless communication antennas," *IEEE microwave magazine*, vol. 4, no. 1, pp. 51–67, 2003.
- [9] A. Yaghjian, "Efficient computation of antenna coupling and fields within the near-field region," *IEEE Transactions on antennas and Propagation*, vol. 30, no. 1, pp. 113–128, 1982.
- [10] Z. Yun and M. F. Iskander, "Ray tracing for radio propagation modeling: Principles and applications," *IEEE access*, vol. 3, pp. 1089–1100, 2015.
- [11] R. Charbonnier, C. Lai, T. Tenoux, D. Caudill, G. Gougeon, J. Senic, C. Gentile, Y. Corre, J. Chuang, and N. Golmie, "Calibration of ray-tracing with diffuse scattering against 28-GHz directional urban channel measurements," *IEEE Transactions on Vehicular Technology*, vol. 69, no. 12, pp. 14264–14276, 2020.
- [12] T. Orekondy, P. Kumar, S. Kadambi, H. Ye, J. Soriaga, and A. Behboodi, "WiNeRT: Towards Neural Ray Tracing for Wireless Channel Modelling and Differentiable Simulations," in *The Eleventh International Conference on Learning Representations*, 2022.
- [13] R. A. Drebin, L. Carpenter, and P. Hanrahan, "Volume rendering," *ACM Siggraph Computer Graphics*, vol. 22, no. 4, pp. 65–74, 1988.
- [14] B. Mildenhall, P. P. Srinivasan, M. Tancik, J. T. Barron, R. Ramamoorthi, and R. Ng, "NeRF: Representing Scenes as Neural Radiance Fields for View Synthesis," in *ECCV*, 2020.
- [15] J. T. Barron, B. Mildenhall, M. Tancik, P. Hedman, R. Martin-Brualla, and P. P. Srinivasan, "Mip-nerf: A multiscale representation for anti-aliasing neural radiance fields," in *Proceedings of the IEEE/CVF international conference on computer vision*, pp. 5855–5864, 2021.
- [16] T. Müller, A. Evans, C. Schied, and A. Keller, "Instant neural graphics primitives with a multiresolution hash encoding," *ACM transactions on graphics (TOG)*, vol. 41, no. 4, pp. 1–15, 2022.
- [17] B. Kerbl, G. Kopanas, T. Leimkühler, and G. Drettakis, "3D Gaussian Splatting for Real-Time Radiance Field Rendering," *ACM Transactions on Graphics*, vol. 42, July 2023.
- [18] H. Xie, Z. Chen, F. Hong, and Z. Liu, "GaussianCity: Generative Gaussian Splatting for Unbounded 3D City Generation," *arXiv preprint arXiv:2406.06526*, 2024.
- [19] W. Sun, X. Zhang, F. Wan, Y. Zhou, Y. Li, Q. Ye, and J. Jiao, "Correspondence-Guided SfM-Free 3D Gaussian Splatting for NVS," *arXiv preprint arXiv:2408.08723*, 2024.
- [20] G. Wu, T. Yi, J. Fang, L. Xie, X. Zhang, W. Wei, W. Liu, Q. Tian, and X. Wang, "4d gaussian splatting for real-time dynamic scene rendering," in *Proceedings of the IEEE/CVF Conference on Computer Vision and Pattern Recognition*, pp. 20310–20320, 2024.
- [21] F. Liu, Y. Cui, C. Masouros, J. Xu, T. X. Han, Y. C. Eldar, and S. Buzzi, "Integrated Sensing and Communications: Toward Dual-Functional Wireless Networks for 6G and Beyond," *IEEE Journal on Selected Areas in Communications*, vol. 40, no. 6, pp. 1728–1767, 2022.
- [22] L. U. Khan, W. Saad, D. Niyato, Z. Han, and C. S. Hong, "Digital-Twin-Enabled 6G: Vision, Architectural Trends, and Future Directions," *IEEE Communications Magazine*, vol. 60, no. 1, pp. 74–80, 2022.
- [23] Y. Lu, X. Huang, K. Zhang, S. Maharjan, and Y. Zhang, "Low-latency federated learning and blockchain for edge association in digital twin empowered 6G networks," *IEEE Transactions on Industrial Informatics*, vol. 17, no. 7, pp. 5098–5107, 2020.
- [24] X. Zhao, Z. An, Q. Pan, and L. Yang, *NeRF2: Neural Radio-Frequency Radiance Fields*. New York, NY, USA: Association for Computing Machinery, 2023.
- [25] A. Medeisis and A. Kajackas, "On the use of the universal Okumura-Hata propagation prediction model in rural areas," in *VTC2000-Spring, 2000 IEEE 51st Vehicular Technology Conference Proceedings (Cat. No. 00CH37026)*, vol. 3, pp. 1815–1818, IEEE, 2000.
- [26] R. Valenzuela, "A ray tracing approach to predicting indoor wireless transmission," in *IEEE 43rd vehicular technology conference*, pp. 214–218, IEEE, 1993.
- [27] J. W. McKown and R. L. Hamilton, "Ray tracing as a design tool for radio networks," *IEEE Network*, vol. 5, no. 6, pp. 27–30, 1991.
- [28] T. Imai, K. Kitao, and M. Inomata, "Radio propagation prediction model using convolutional neural networks by deep learning," in *2019 13th European Conference on Antennas and Propagation (EuCAP)*, pp. 1–5, IEEE, 2019.
- [29] A. Kamari, Y. Chae, and P. Pathak, "mmSV: mmWave Vehicular Networking using Street View Imagery in Urban Environments," in *Proceedings of the 29th Annual International Conference on Mobile Computing and Networking*, pp. 1–16, 2023.
- [30] R. Levie, Ç. Yapar, G. Kutyniok, and G. Caire, "RadioUNet: Fast radio map estimation with convolutional neural networks," *IEEE Transactions on Wireless Communications*, vol. 20, no. 6, pp. 4001–4015, 2021.
- [31] S. Bakirtzis, J. Chen, K. Qiu, J. Zhang, and I. Wassell, "EM DeepRay: an expedient, generalizable, and realistic data-driven indoor propagation model," *IEEE Transactions on Antennas and Propagation*, vol. 70, no. 6, pp. 4140–4154, 2022.
- [32] G. Cao and Z. Peng, "RayProNet: A Neural Point Field Framework for Radio Propagation Modeling in 3D Environments," *arXiv preprint arXiv:2406.16907*, 2024.
- [33] A. Rose, "The sensitivity performance of the human eye on an absolute scale," *JOSA*, vol. 38, no. 2, pp. 196–208, 1948.
- [34] C. Gentile, J. Senic, A. Bodi, S. Berweger, R. Caromi, and N. Golmie, "Context-Aware Channel Sounder for AI-Assisted Radio-Frequency Channel Modeling," in *2024 18th European Conference on Antennas and Propagation (EuCAP)*, pp. 1–5, 2024.
- [35] J. Hoydis, S. Cammerer, F. A. Aoudia, A. Vem, N. Binder, G. Marcus, and A. Keller, "Sionna: An open-source library for next-generation physical layer research," *arXiv preprint arXiv:2203.11854*, 2022.
- [36] J. Hoydis, F. A. Aoudia, S. Cammerer, M. Nimier-David, N. Binder, G. Marcus, and A. Keller, "Sionna RT: Differentiable ray tracing for radio propagation modeling," in *2023 IEEE Globecom Workshops (GC Wkshps)*, pp. 317–321, IEEE, 2023.
- [37] H. L. Van Trees, *Optimum array processing: Part IV of detection, estimation, and modulation theory*. John Wiley & Sons, 2002.
- [38] M. S. Bartlett, "Periodogram analysis and continuous spectra," *Biometrika*, vol. 37, no. 1/2, pp. 1–16, 1950.
- [39] T. Lauer, "Deconvolution with a spatially variant PSF," in *Astronomical data analysis II*, vol. 4847, pp. 167–173, SPIE, 2002.
- [40] J. Capon, "High-resolution frequency-wavenumber spectrum analysis," *Proceedings of the IEEE*, vol. 57, no. 8, pp. 1408–1418, 1969.
- [41] J. A. Fessler and A. O. Hero, "Space-alternating generalized expectation-maximization algorithm," *IEEE Transactions on signal processing*, vol. 42, no. 10, pp. 2664–2677, 1994.
- [42] J. Verhaevert, E. Van Lil, and A. Van de Capelle, "Direction of arrival (DOA) parameter estimation with the SAGE algorithm," *signal processing*, vol. 84, no. 3, pp. 619–629, 2004.
- [43] P. B. Papazian, J.-K. Choi, J. Senic, P. Jeavons, C. Gentile, N. Golmie, R. Sun, D. Novotny, and K. A. Remley, "Calibration of millimeter-wave channel sounders for super-resolution multipath component extraction," in *2016 10th European Conference on Antennas and Propagation (EuCAP)*, pp. 1–5, 2016.
- [44] R. Zhang, P. Isola, A. A. Efros, E. Shechtman, and O. Wang, "The unreasonable effectiveness of deep features as a perceptual metric," in *Proceedings of the IEEE conference on computer vision and pattern recognition*, pp. 586–595, 2018.
- [45] W. Lin and C.-C. J. Kuo, "Perceptual visual quality metrics: A survey," *Journal of visual communication and image representation*, vol. 22, no. 4, pp. 297–312, 2011.
- [46] M. Mirza and S. Osindero, "Conditional generative adversarial nets," *arXiv preprint arXiv:1411.1784*, 2014.
- [47] Y. He, Y. Chen, Y. Hu, and B. Zeng, "WiFi Vision: Sensing, Recognition, and Detection With Commodity MIMO-OFDM WiFi," *IEEE Internet of Things Journal*, vol. 7, no. 9, pp. 8296–8317, 2020.
- [48] Y. Ma, G. Zhou, and S. Wang, "WiFi Sensing with Channel State Information: A Survey," *ACM Comput. Surv.*, vol. 52, jun 2019.